Microstructural evolution and strengthening mechanisms of a high-strength Al-Mg-Si alloy processed by laser powder bed fusion and ageing treatment

Tao Wen[a], Jianying Wang[a], Zhicheng Li[a], Feipeng Yang[a], Zhilin Liu[b], Hailin Yang[a,*], Shouxun Ji[c]

a. State Key Laboratory of Powder Metallurgy, Central South University, Changsha 410083, China

b Light Alloy Research Institute, College of Mechanical and Electrical Engineering, Central South University, Changsha, 410083, China

c. Brunel Centre for Advanced Solidification Technology (BCAST), Brunel University London, Uxbridge, Middlesex, UB8 3PH, United Kingdom

* Corresponding authors: y-hailin@csu.edu.cn

Abstract: In this work, the microstructural evolution and mechanical properties of a novel Al-5.3 wt.% Mg-3.3 wt.% Si alloy fabricated by laser powder bed fusion (LPBF) were investigated systematically. The results confirmed the formation of hierarchical microstructures, featured by the fine α-Al matrix that contains the interaction between the nanosized Mg_2Si eutectic and the high-density dislocations in the as-LPBFed crack-free Al-5.3 wt.% Mg-3.3wt.% Si alloy. The alloy delivers the yield strength of 374 MPa and the elongation of 5.8 % Under as-LPBFed condition. The yield strength is further enhanced to 432 MPa under as-aged condition processed at 180 °C for 6 h. The property enhancement is closely linked to the precipitation of β″ and β phases. However, the broken and coarsened Mg_2Si eutectics and the reduction of dislocation density result in strength degradation after ageing exceeds 300 °C.

Keywords: Aluminium alloys; Microstructure; Mechanical properties; Laser powder bed fusion; Heat treatment.

1 Introduction

Additive manufacturing (AM) technology has attracted significant interest for its ability to rapidly fabricate geometrically complex components with the high design freedom [1-3]. Currently, laser powder bed fusion (LPBF), one of the most popular AM technologies, has a huge potential for the applications in aerospace, automobile and biology [4, 5]. However, LPBF of aluminium (Al) alloys faces a series of significant challenges, such as low laser energy absorption, high thermal conductivity and oxidation during processing [6-8]. The proven Al alloys for LPBF are mainly limited to the near eutectic cast Al-Si alloys (e.g. Al12Si, AlSi10Mg, AlSi7Mg) [5, 9-12], which can offer the ultimate tensile strength (UTS) at a level of 400 MPa and the ductility at a level of 4%. Moreover, severe cracking in the LPBFed 2xxx (Al-Cu), 6xxx (Al-Mg-Si) and 7xxx (Al-Zn-Mg-Cu) wrought alloys have limited their industrial applications[13, 14]. Although previous studies have suggested that optimized process parameters can increase the relative density, the cracking was still hard to be solved satisfactorily [15, 16].

Currently, the introduction of grain refiner to as-LPBFed Al alloys is an effective strategy to reduce cracking susceptibility and improve processability. It is reported that the Sc/Zr addition in as-LPBFed Al-8.0Mg-1.3Si alloy exhibited a low hot cracking susceptibility and superior mechanical properties (UTS of 497 MPa and El of 11%) [17]. Similarly, the addition of nano-sized ceramic particles into Al-Mg-Si alloy, such as TiC [18], and/or Zr_2O[19], promoted the columnar to equiaxial transition and increased the nucleation sites of α-Al grains. However, the additions of extra Sc/Zr and particle-modified powders normally have no advantages in terms of cost control and large-scale industrial applications. Recently, a few studies indicated that the tailored Mg and Si contents can offer huge potential for eliminating the hot tearing in the as-LPBFed Al-Mg-Si alloys. For example, the granular Mg_2Si and rod-shaped Si particles in crack-free Al-Mg-Si alloy with 4.4 wt.% Mg and 3.1 wt.% Si delivered the high UTS of 460 MPa and elongation of 3.2 % under as-LPBFed condition [20]. Additionally, a newly designed Al-9.6 wt.% Mg-4.9 wt.% Si alloy can achieve the UTS of 557 MPa and elongation of 2.9 % [21].

Also, the heat treatment is an effective method to alter the mechanical properties of the as-LPBFed Al alloys via tuning cellular structures and/or promoting the formation of precipitates [22-25]. Normally, the conventional T6 treatment with a relatively short solution time was applied to remediate the brittleness of as-LPBFed Al-Si and Al-Mg-Si based alloys. For example, the AlSi10Mg alloys with solution treatment at 550 °C for 2 h can decrease the UTS from 434 MPa to 168 MPa, while the elongation increases from 5.3% to 23.7% [23]. In

comparison, the direct ageing treatment serves as a novel and promising method to achieve a trade-off between strength and ductility via maintaining the cellular structure and promoting the formation of precipitation phase. It is worth noting that the precipitation of fine Si particles during ageing process in the AlSi10Mg alloy promotes strength enhancement [24]. Similarly, the precipitation of β′′ nanoparticles within α-Al cells induced from ageing was attributed to the strength enhancement in the as-LPBFed AlSi8.1Mg1.4 alloy [25]. For the widely-studied as-LPBFed Al-Mg-Si-Sc-Zr alloy with ageing treatment at 300 ~ 400 °C, the formation of Al_3(Sc, Zr) nanoprecipitates can improve strength effectively [17]. However, the studies about the ageing treatment of printable Al-Mg-Si alloy without the addition of extra Sc/Zr and particle-modified was have not yet been reported, and it is important to design a novel strength-ductility synergy of as-LPBFed Al-Mg-Si alloy and understand the effects of ageing treatment on the microstructural evolution and mechanical properties thoroughly.

Currently, the challenges of as-LPBFed Al alloy focus on their processability, strength and cost. On the basis of abandoning the addition of Sc/Zr and nanoparticle modification, this work is devoted to compositional regulation based on the Al6061 alloy system with high crack susceptibility. Therefore, the processability, microstructure and mechanical properties of a novel Al-5.3 wt.% Mg-3.3 wt.% Si processed via LPBF were investigated systematically. Meanwhile, the characterization of the microstructural evolution and mechanical properties are evaluated under ageing treatment. Discussion focuses on the fundamentals for lowering hot-cracking susceptibility, microstructural evolution and the contribution of strengthening mechanisms.

2. Experimental

2.1 Powder and materials fabrication

Al-5.3Mg-3.3Si pre-alloyed powders were prepared by gas atomization. The chemical compositions of the alloyed powders and as-LPBFed sample shown in **Table 1** were measured using inductively coupled plasma atomic emission spectrometry (ICAP 7000 Series, Waltham, USA). **Fig. 1** shows the powder morphology, particle size distribution and elemental distribution mapping. The size distribution of spherical particles was measured as 9.5 ~ 73.6 μm with the mean size of 29.7 μm. Meanwhile, the EDS mapping confirmed that there was no obvious elemental segregation in the Al-5.3Mg-3.3Si powders.

The LPBF with an IPG Fiber Laser was applied to fabricate Al-5.3Mg-3.3Si samples for microstructural characterization and mechanical property testing. The laser scanning was rotated 67° layer-by-layer, as shown in **Fig. 2a**. The processing parameters included the laser powder (*P*) of 270, 290, 310, 330, 350, 370 W, the scan speed (*v*) of 600, 800, 1000, 1200,

1400 mm/s, the hatch spacing (*h*) of 0.1 mm, layer thickness (*t*) of 0.03 mm. The samples were built on a substrate plate of AlSi10Mg alloy. The size of cubic samples and cuboid samples were 10 mm × 10 mm × 10 mm and 60 mm × 10 mm ×10 mm, respectively. The relative density of samples was measured by the Archimedes method. The dog-bone-shaped sample for the test with a spacing length of 20 mm and a cross-section of 4 × 2 mm^2 is schematically shown in **Fig. 2d**. The ageing treatment was performed at 160 ºC, 180 ºC, 200 ºC, 250 ºC and 300 ºC for 1 ~ 8 h followed by air cooling.

Table 1. Chemical compositions of the Al-5.3Mg-3.3Si powders and as-LPBFed sample measured by ICP-AES (wt.%).

Alloy	Mg	Si	Mn	Fe	Others	Al
Powder	5.34	3.27	0.68	0.22	<0.08	Bal.
LPBFed sample	5.22	3.25	0.64	0.21	<0.08	Bal.

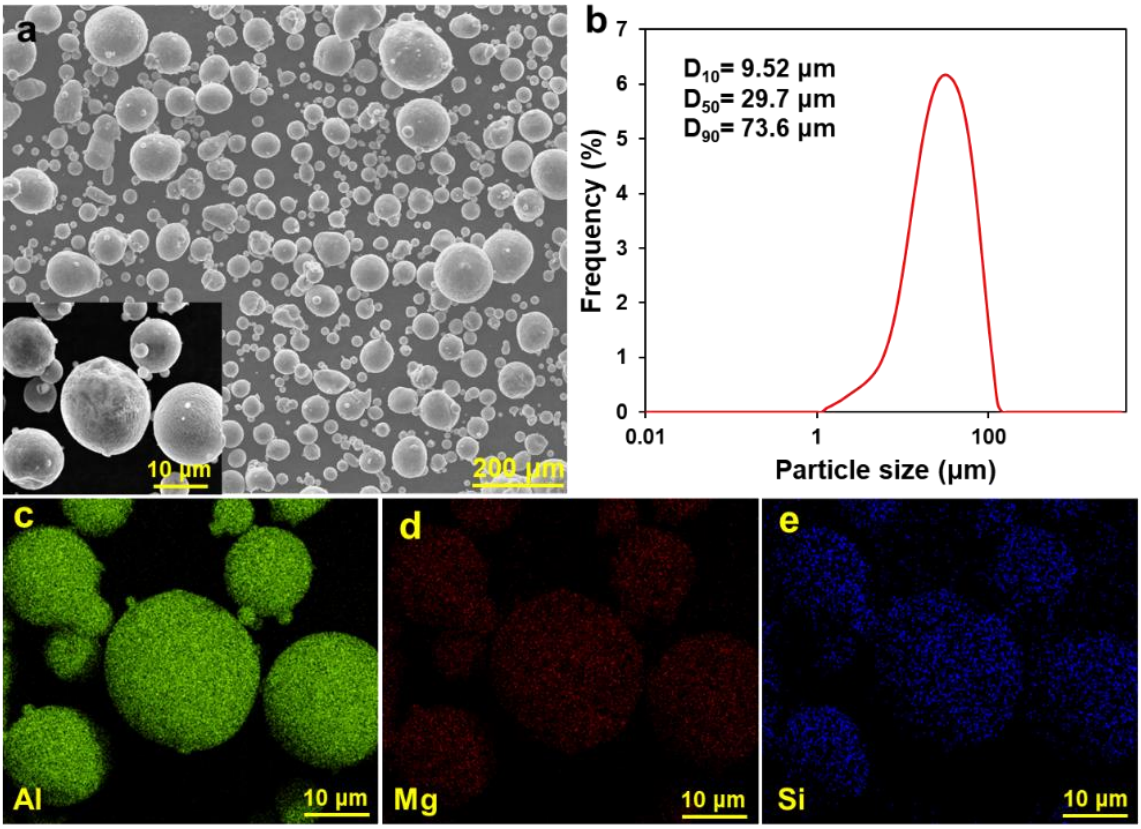

Fig. 1. Characterization of Al-5.3Mg-3.3Si powder: (a) Powder particle morphology; (b) Particle size distribution of the atomized powder; (c-e) EDS mapping for elemental distribution.

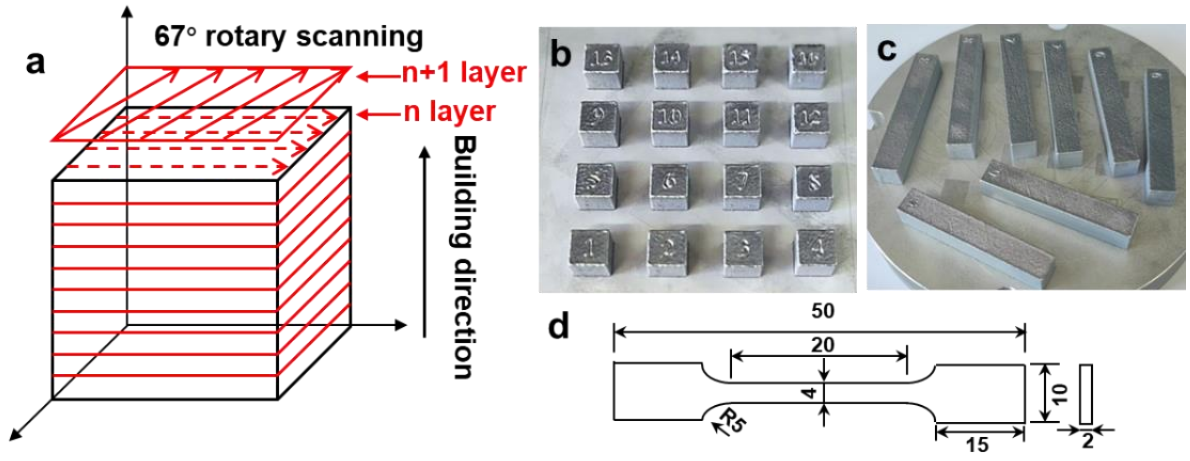

Fig. 2. (a) Schematic of the scanning strategy during LPBF process; (b) the cubic samples; (c) the cuboid samples; and (d) the dimension of dog-bone-shaped tensile samples.

2.2 Microstructural characterization

The defects of samples under different conditions were characterized via Leica DM4000M optical microscope (OM). Microstructures were observed using a scanning electron microscope (SEM, Quanta 250 FEG), and samples were etched with Keller's solution before SEM observation. The grain size and grain orientation were characterized using an electron backscattered diffraction (EBSD, Helios NaboLab G3 UC). Furthermore, the detailed microstructure analysis was conducted using a transmission electron microscope (TEM, Talos F200X). TEM samples were prepared by a precision ion polishing system (PIPS, Gatan691) at a voltage of 5 kV and an incident angle of 3 ~ 8°. The phase constituent of samples was identified using X-ray diffraction with Cu *K*α radiation (XRD, Rigaku X-2000). Additionally, the dislocation density was estimated from the XRD results through the Williamson-Hall method[26], which describes that the broadening of the diffraction peak (β) incorporates two parts, namely, the crystallite size broadening (β_G) and the strain broadening (βs). Based on the assumption of a Cauchy-type function, β is calculated as[27]:

$$\beta=\beta_G+\beta_S \quad (1)$$

$$\beta_G=K\lambda / (D\times\cos\theta) \quad (2)$$

$$\beta_S=4\varepsilon\times\tan\theta \quad (3)$$

where K is a constant (0.9), λ is the wavelength of Cu-$K\alpha$ radiation (0.15405 nm), D is the crystallite size, ε is the micro strain, θ and is the Bragg angle of the specific diffraction peak[26]. Therefore, equation (4) is shown below:

$$\beta\times cos\theta= K\lambda/D+(4sin\theta)\times\varepsilon \quad (4)$$

According to Eq. (5), ε can be evaluated from the slope of the linear fit of the $\beta\cos\theta$-$4\sin\theta$ data. b is the Burgers vector (0.286 nm[26]). The dislocation density (ρ) can be obtained by the following equation:

$$\rho=2\sqrt{3}\varepsilon/(Db) \qquad (5)$$

2.3 Mechanical properties testing

The micro-hardness was tested by a micro-Vickers hardness instrument (ASTME 384-08) with 200 g load for 15 s, and the average value was taken from at least 10 points of each sample. The dog-bone-shaped tensile samples were cut by electrical discharge machining (EDM) from the as-LPBFed samples. Uniaxial tensile tests were performed using a testing system (MTS, Alliance RT30) with an engineering strain rate of 1×10^{-3} s^{-1} at room temperature (RT). The tensile data were the average of three measurements.

3. Results

3.1 Densification behaviour

Fig. 3 shows the densification behaviours of as-LBPFed Al-5.3Mg-3.3Si samples obtained at different volumetric energy densities (*VEDs*). The relative density increased with increasing the *VED*, and the porosity fraction shows an opposite trend. The relative density remained above 99.5% and the porosity fraction remained at ~ 0.5% with the increase of *VED* to 129.1 J/mm^3. Particularly, the relative density can achieve 99.6% under the condition of 103.3 J/mm^3. However, the relative density decreased from 99.5% to 98.1% with the increase of *VED* from 129.1 to 205.5 J/mm^3. Meanwhile, the characteristics of defects are shown in **Fig. 3c.** It can be seen that insufficient *VEDs* led to the formation of a few of un-melted powders. With the increase of *VED*, the liquid metal mobility and wettability were improved obviously. In these conditions, only a trace of gas pores was detected in the samples. When the *VED* was further increased, the molten metal is too late to fill the pores, the formation of keyhole led to the poor relative density.

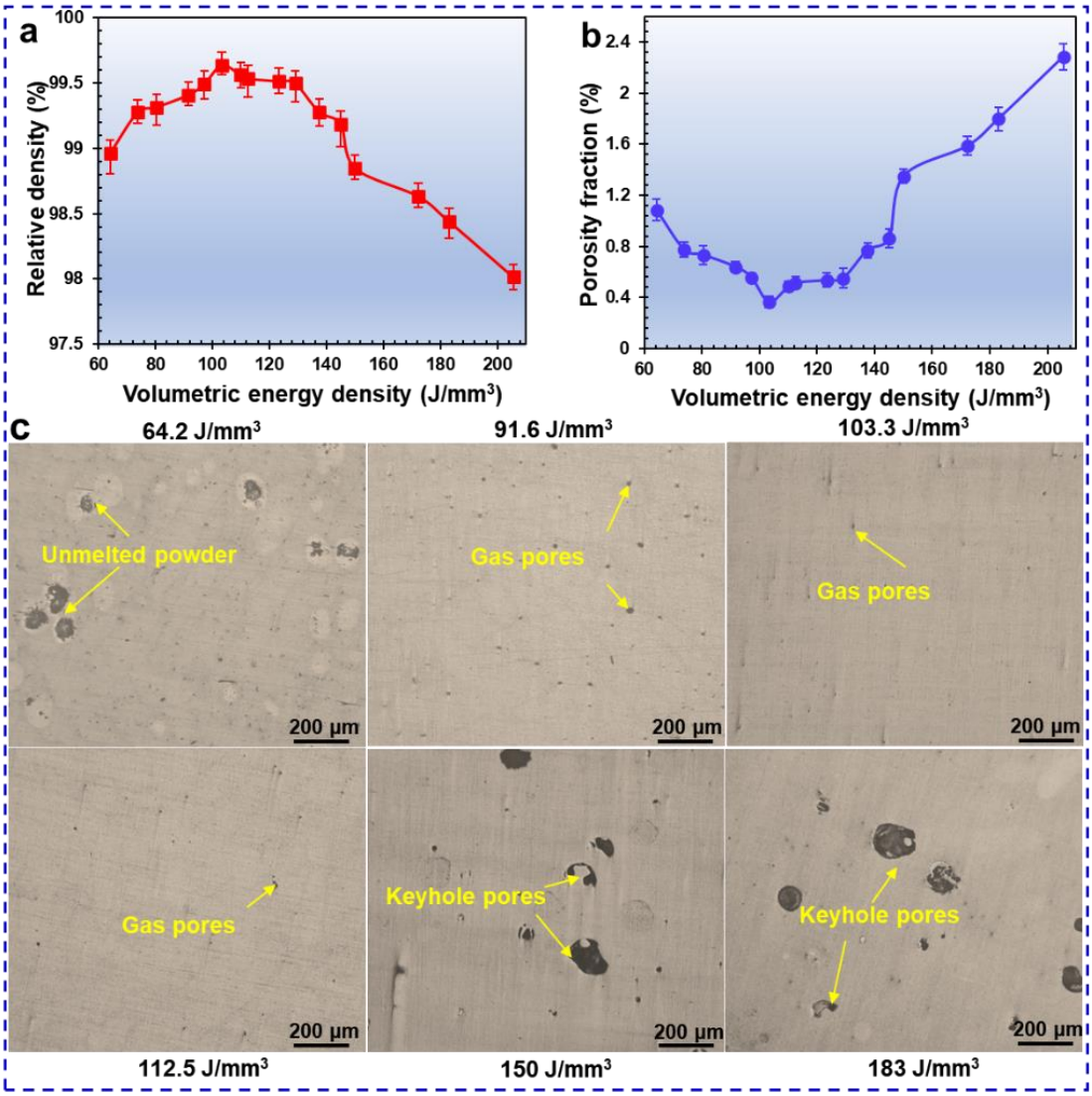

Fig. 3. Densification behaviours of as-LBPFed Al-5.3Mg-3.3Si samples obtained at different *VEDs*: (a) The relative density and (b) The porosity fraction; (c) Optical micrographs showing the distribution and morphology of defects.

3.3 Microstructural characterization

Fig. 4 shows the microstructure of as-LPBFed Al-5.3Mg-3.3Si samples. In the horizontal section, some continuous laser tracks were formed with 67° rotating scanning (**Fig. 4a**). In **Fig. 4b**, the melt pool (MP) was composed of the heat affected zone (HAZ), MP coarse zone and MP fine zone. The HAZ was regarded as the transition zone between the MP fine zone and MP coarse zone. The eutectic cellular structures with the average size of 0.39 μm were featured by α-Al phases and eutectic Mg_2Si particles (**Fig. 4c**). The grain size and texture of as-LBPFed Al-5.3Mg-3.3Si alloy were further analysed via EBSD. The inverse pole figure (IPF) map in **Fig. 4d** was characterized by numerous equiaxed grains, and the average grain size was 12.1 μm (**Fig. 4e**). Meanwhile, the pole figures colour demonstrates of the alloy showed a strong {001} texture.

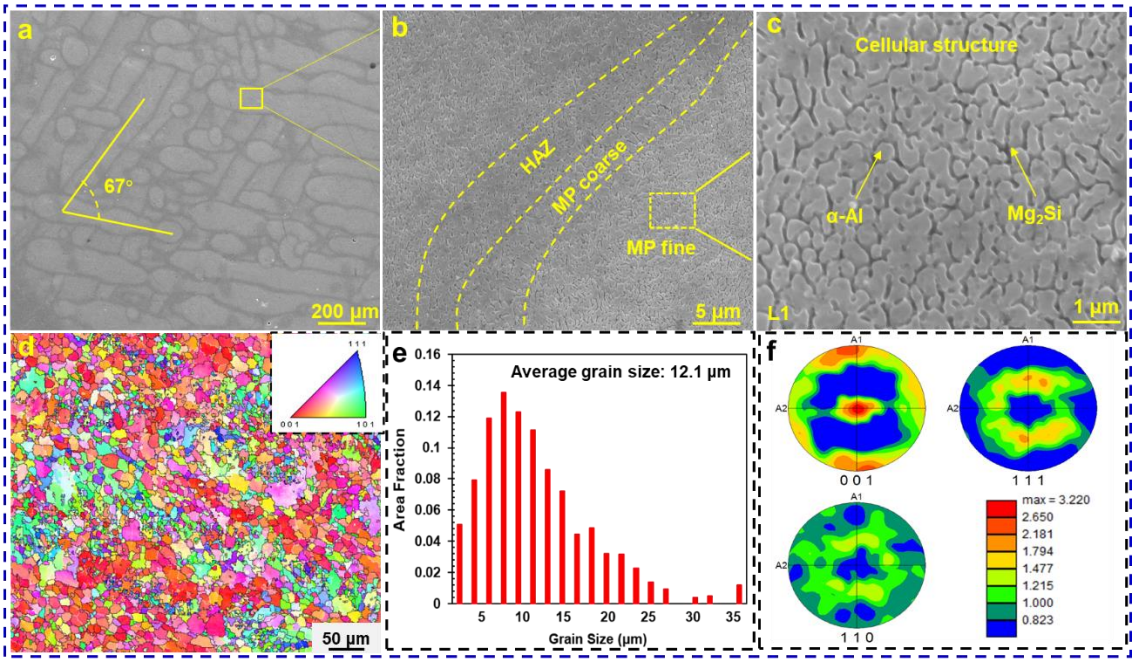

Fig. 4. The microstructure of the as-LBPFed Al-5.3Mg-3.3Si alloy; (a, b) characteristic of melt pool structure; (c) cellular structure; (d) inversed pole figure (IPF) maps; (e) grain size distribution; and (f) the {001} pole figures.

TEM images along the [011] zones axis showed the detailed microstructure of as-LPBFed Al-5.3Mg-3.3Si alloy further, as shown in **Fig. 5**. Similar to SEM result in Fig. 4c, a large number of cellular structures were uniformly distributed in **Fig. 5a**. High angle annular dark field-scanning TEM image (HAADF-STEM, **Fig. 5d**) and the detailed element distribution (Figs. **5d$_1$-d$_5$**) indicated that Mg and Si mainly distributed at the boundaries of cellular structures, confirming the formation of divorced Al/Mg_2Si eutectics. Meanwhile, it is noticed that Fe and Mn were segregated together with Mg_2Si particles, and the Fe/Mn-rich phase consisted of Al, Fe, Mn and Si. Also, the interaction between dislocations and distinct eutectic network that contains nano-sized Mg_2Si particles are illustrated in **Figs. 5b-c**.

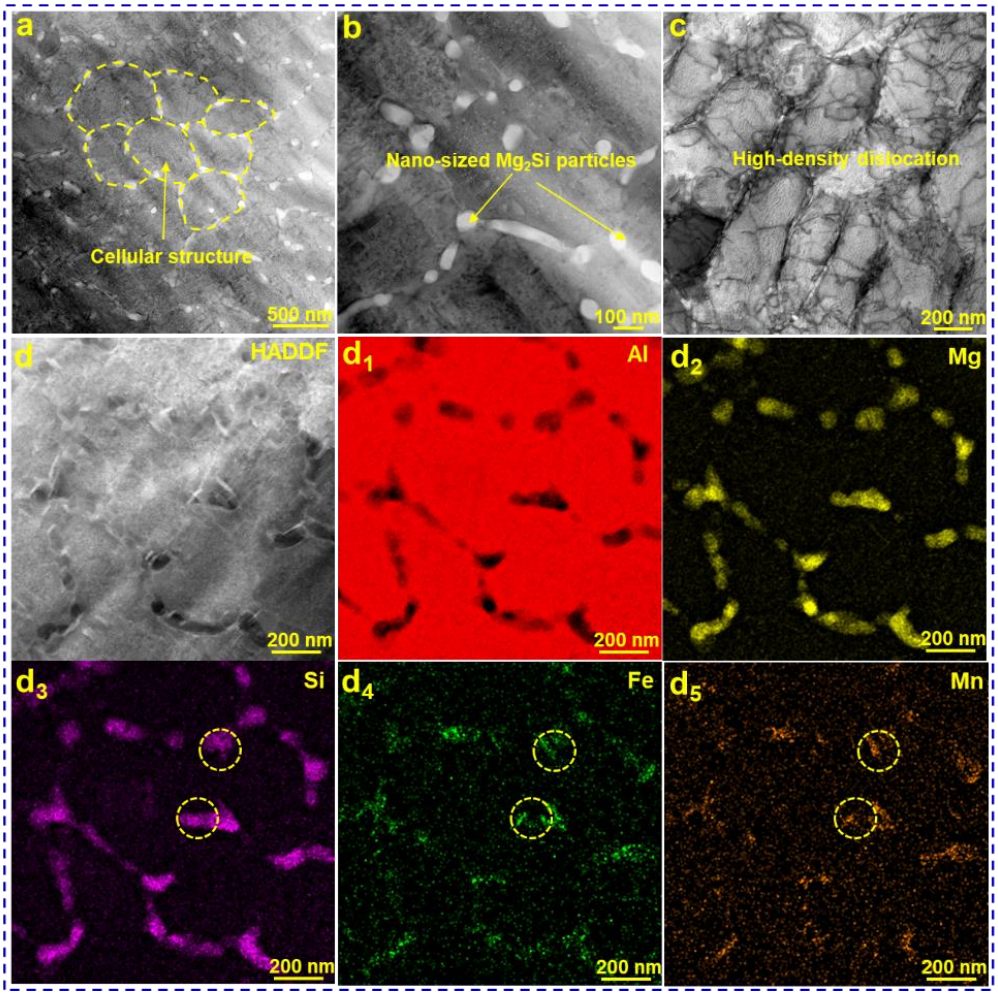

Fig. 5 TEM micrographs showing the microstructure of as-LPBFed Al-5.3Mg-3.3Si alloy, (a) BF-TEM images of the typical cellular structure, (b) nano-sized Mg_2Si particles, (c) high-density dislocation with the cellular structure, (d) HAADF-STEM image showing the cellular structure, and corresponding mapping of main elements of Al, Mg, Si, Fe, Mn.

To further investigate the orientation relationship (OR) between α-Al matrix, Mg_2Si and Fe/Mn enriched particles, high-resolution TEM (HR-TEM) and fast Fourier transform (FFT) images are shown in **Fig. 6.** The interface characteristics between α-Al matrix and Mg_2Si phase are shown in **Figs. 6a-b**. The Al/Mg_2Si showed a coherent orientation relationship (OR) with $(200)_{\alpha\text{-Al}}//(\bar{1}1\bar{1})_{Mg2Si}$, $[001]_{\alpha\text{-Al}}//[\bar{1}12]_{Mg2Si,}$ and the interplanar spacing of Mg_2Si was 0.363 nm for $(\bar{1}1\bar{1})$ (**Fig. 6c**). Meanwhile, the Fe/Mn-enriched phase was determined as α-AlFeMnSi, clarified by the HR-TEM and FFT images (**Figs. 6d-e**). The OR between α-Al and α-AlFeMnSi particles could be described as $(\bar{1}1\bar{1})_{\alpha\text{-Al}}//(02\bar{2})_{\alpha\text{-AlFeMnSi}}$, $(\bar{2}00)_{\alpha\text{-Al}}//(42\bar{2})_{\alpha\text{-AlFeMnSi}}$, and $[011]_{\alpha\text{-Al}}//[\bar{1}22]_{\alpha\text{-AlFeMnSi}}$. The interplanar spacing of α-AlFeMnSi particle was 0.915 nm for $(02\bar{2})$ (**Figs. 6f**). Also, the β″ phase with 5 ~ 10 nm was found within the cellular structure in **Fig. 6g**, which was consistent with previous literature [25].

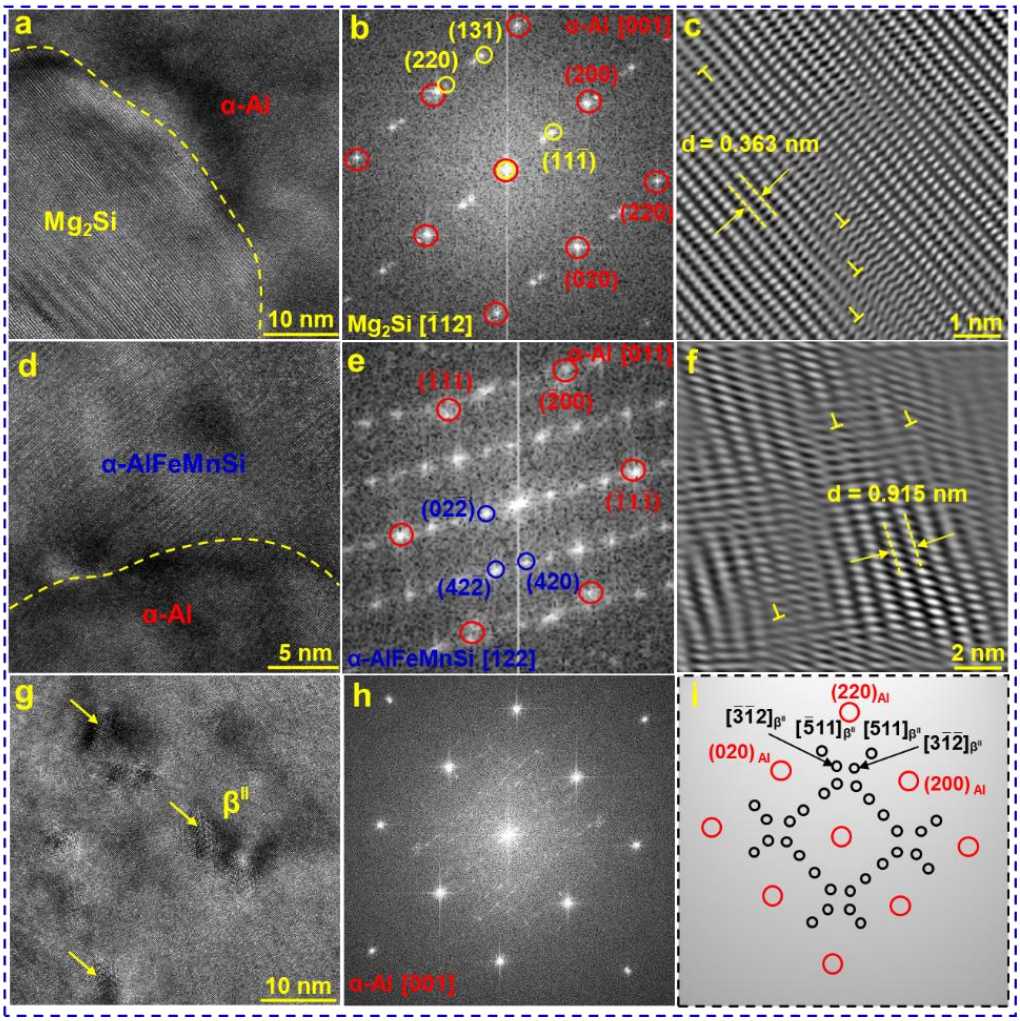

Fig. 6. (a) HR-TEM image of the α-Al and Mg_2Si phase, taken along the [001]0 zone axis, (b) FFT image of the marked area in (a); (c) the interplanar spacing of Mg_2Si and high-density dislocations (marked by "T"); (d) HR-TEM image of the α-Al and α-AlFeMnSi, taken along the [011] zone axis; ; (e) FFT image of the marked area in (d); (f) the interplanar spacing of α-AlFeMnSi and high-density dislocations; (g) the β″ phase in the cellular structure and (h, i) corresponding SAED patterns.

3.2 Effect of direct ageing on the microstructural evolution

The microstructural characteristics of Al-5.3Mg-3.3Si alloy without and with direct ageing are shown in **Fig. 7**. It is worth noting that the cellular structure remained good stability under the conditions of ageing at 160 °C and 180 °C, almost identical to the typical microstructure of the as-LPBFed sample (**Figs. 7a-c**). Based on the statistical results, the average size of cellular structure was increased from 0.39 μm to 0.56 μm after ageing at 180 °C for 6 h. After ageing at 200 °C for 3 h, the enlarged cellular structure was partially dissolved and the precipitation of Mg_2Si particles was detected inside the cellular structures (**Fig. 7d**). As the ageing temperature increases to 250 °C further, the cellular structure was completely dissolved and the coarsened Mg_2Si particles was homogeneously distributed in the α-Al matrix. Specifically, the size Mg_2Si particles reached to ~350 nm after ageing at 300 °C for 3

h (**Fig. 7f**). Furthermore, the grain morphologies of α-Al grains and grain size distribution in as-aged samples are shown in **Fig. 8**. It can be seen that the α-Al grains of the as-aged samples has not changed significantly in comparison to the as-LPBFed samples. The average grain size of α-Al grains was 11.9 μm and 12.7 μm after as-aged at 180 °C and 300 °C, respectively.

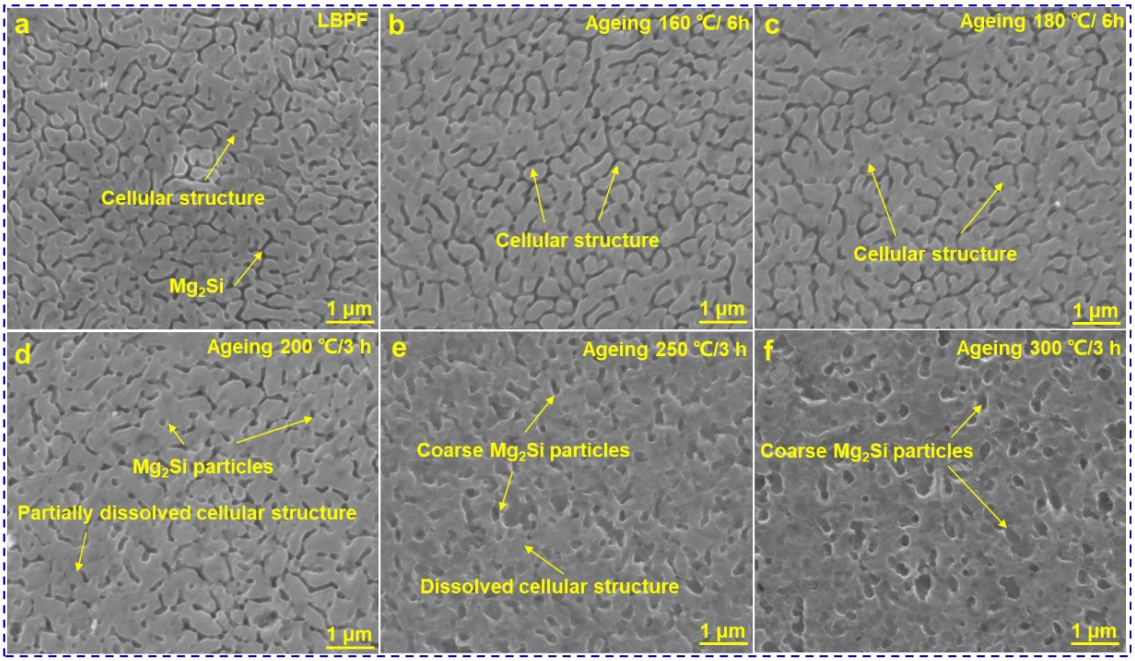

Fig. 7. SEM images of Al-5.3Mg-3.3Si alloy under different conditions: (a) as-LPBFed, (b) aged at 160 ºC for 6 h, (c) aged at 180 ºC for 6 h, (d) aged at 200 ºC for 3 h, (e) aged at 250 ºC for 3 h and (f) aged at 300 ºC for 3 h.

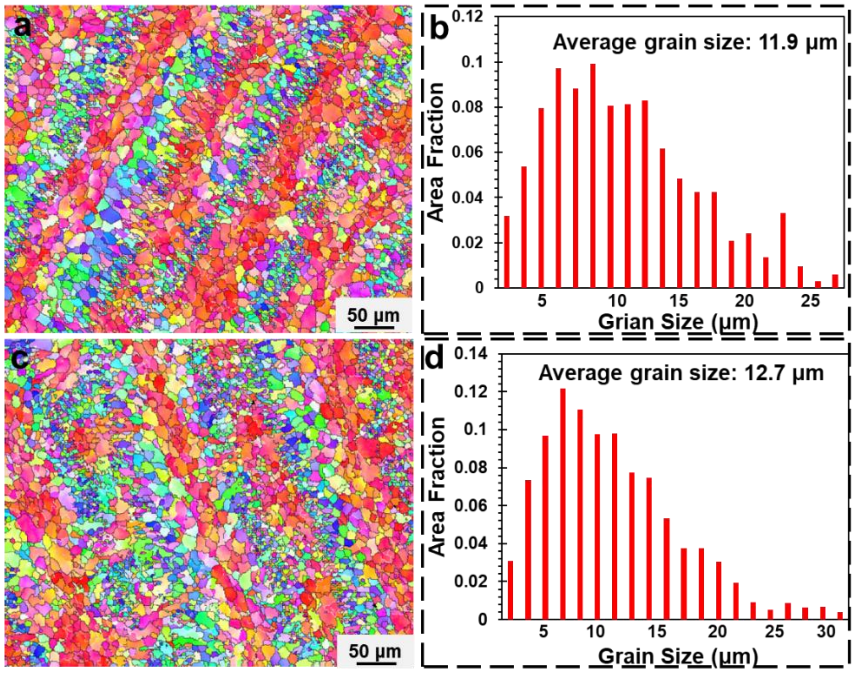

Fig. 8. The EBSD-IPF maps and grain size distribution: (a, b) as-aged at 180 °C; (c, d) as-aged at 300 °C.

TEM analysis was applied to further investigate the detailed microstructure of the as-aged sample (180 °C for 6 h), and the results are shown in **Fig. 9**. Similar to the result of SEM, the remained cellular structure could be detected in **Fig. 9a**. Meanwhile, the interactions between dislocation and β″/β phase were observed in **Fig. 9b**. The β″ phase was the main precipitate in the Al-Mg-Si alloy under peak ageing condition, which presented the C-centred monoclinic structure with a = 1.506 nm, c = 0.671 nm[28]. As shown in **Fig. 6g**, a trace of β″ phase has already been found in as-LPBFed sample, and the size of β″ precipitates was further increased to 10~30 nm after ageing treatment (**Fig. 9b&c**). The OR between α-Al and β″ phase particles could be described as $(020)_{\alpha\text{-Al}}//(020)_{\beta''}$, $(200)_{\alpha\text{-Al}}//(10\bar{6})_{\beta''}$, as verified in the FFT pattern of **Fig. 9d**. Meanwhile, HR-TEM image and FFT pattern in **Fig. 9e** and **9f** indicated that the formation of β phase, and the reflections of $[001]_{\alpha\text{-Al}}$ and $[001]_{\beta}$ could be found and marked in these spots (**Fig. 9f**), which is in accordance with the results of literature [29]. The formation of β phase was found as a result of transformation of β″ phase during ageing.

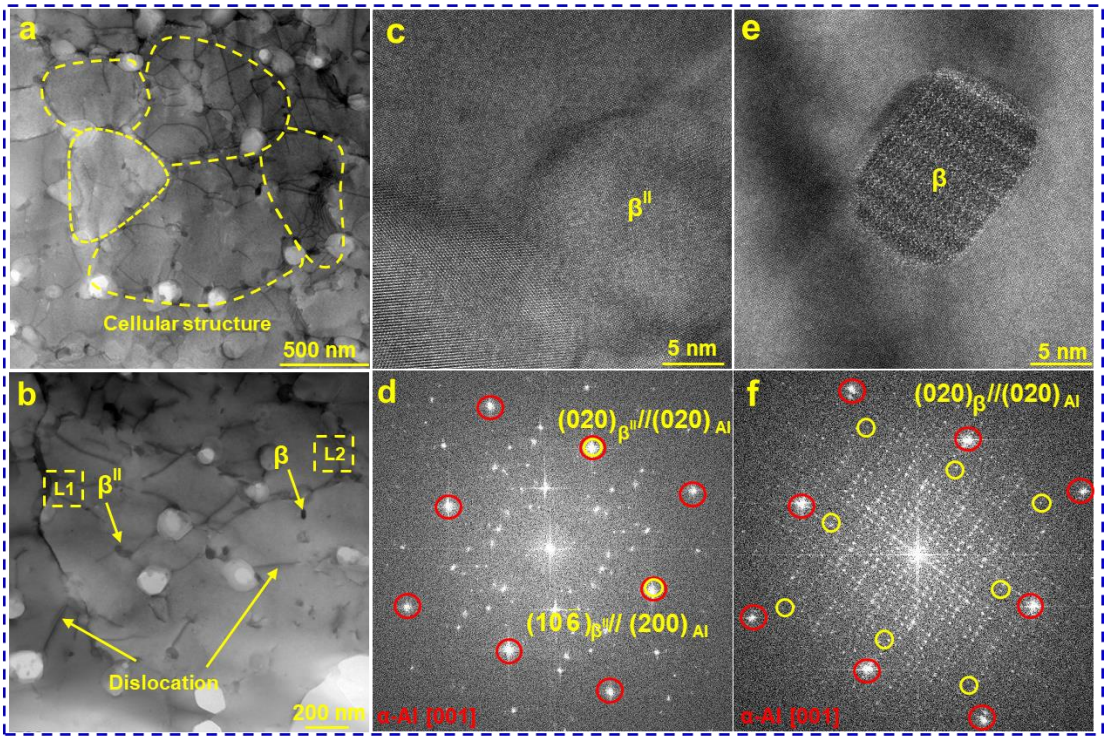

Fig. 9. Detailed TEM images showing the microstructure of the direct aged sample at 180 °C for 6 h; (a) BF-TEM image showing the cellular structure; (b) BF-TEM image the β″and β phase with dislocation; (c, d) HRTEM images of the β″ phase, corresponding FFT image; (e, f) the β phase and corresponding FFT image.

Fig. 10 shows the XRD spectra of the Al-5.3Mg-3.3Si alloy without and with direct ageing. It is seen that α-Al and Mg_2Si phases were clearly visible in all samples. The $(111)_{Al}$ of lattice spacing of as-LPBFed and as-aged sample treated at 180 °C and 300 °C were calculated by

Bragg's law. The results indicated that the lattice spacing in three states are 2.489 nm, 2.476 nm and 2.479 nm, in counterpart with pure Al (2.338 nm). Due to the rapid solidification of LPBF processing, the supersaturated solid solution of Mg and Si tend to form in α-Al matrix, as shown in **Table.2**. Correspondingly, the lattice spacing of the sample in the as-LPBFed sample is larger than that of pure Al. Moreover, β″/β phase and coarse Mg_2Si start to precipitate from the supersaturated matrix during aging (**Fig. 7&9**), which induces a decrease in the lattice spacing of α-Al matrix. According to Bragg's law, the decrease of d leads to the increase of 2θ, which led to the shift of (111) peak to the high angle. Based on equation (1-5), the high dislocation densities (7.1×10^{14} m^{-2}) were formed in the as-LPBFed sample, then decreased slightly when the sample aged at 180 °C for 6 h (6.2×10^{14} m^{-2}). With the increase of ageing temperature to 300 °C for 3 h, the dislocation density reduced to 4.2×10^{14} m^{-2}.

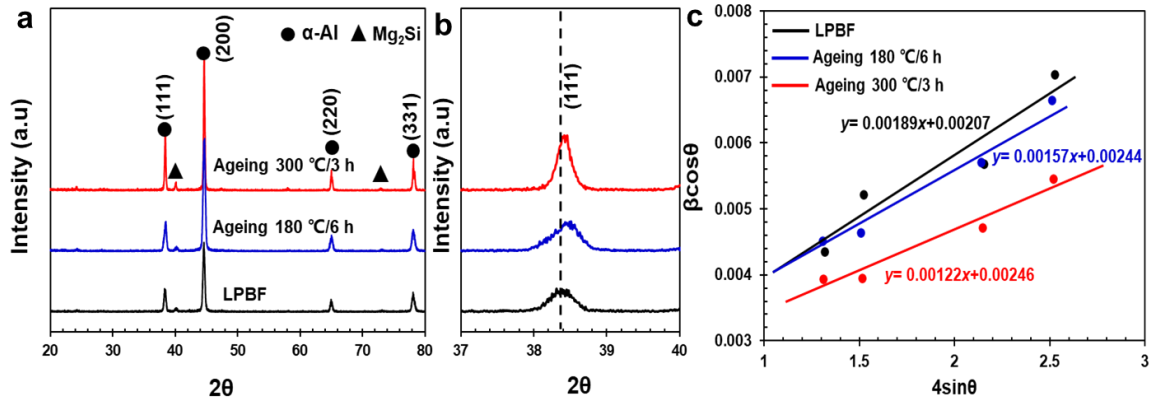

Fig. 10. XRD spectra of as-LPBFed Al-5.3Mg-3.3Si alloy under different direct ageing conditions of 180 °C/6 h and 300 °C/3 h; (b) details near the (111) peak in (a); (c) the *βcosθ*-4*sinθ* plots and the corresponding linear fits.

Table. 2 The content of Al, Mg and Si in the α-Al matrix for the as-LPBFed and as-aged samples measured by semi-quantitative STEM-EDS (wt.%).

Alloy	Mg	Si	Al
as-LPBFed	2.2	1.9	Bal.
as-aged at 180 °C	0.8	0.6	Bal.

3.4 Mechanical properties

Fig. 11a shows the Vickers hardness of as-LPBFed Al-5.3Mg-3.3Si alloy under different ageing conditions. The microhardness of as-LPBFed samples was 170.8 Hv. After ageing at 160 °C and 180 °C, the hardness increased with prolonged ageing to reach the peaks at 177.8 Hv and 179.2 Hv for 6 h, and then decreased with further prolonged ageing. However, the

hardness of samples aged at high temperatures, including 200 °C, 250 °C and 300 °C, decreased continuously with prolonged ageing. Meanwhile, the stress-strain curves of the samples are shown in **Fig. 11b**, and the corresponding data for YS, UTS and El are summarized in **Table 3**. The YS, UTS and El of the as-LPBFed alloy were 374 MPa, 452 MPa and 5.8 %, respectively. After ageing at optimal condition of 180 ºC for 6 h, the YS and UTS increased to 433 MPa and 487 MPa while the El decreased to 2.6%. The as-LPBFed Al-5.3Mg-3.3Si alloy exhibited a significant improvement in mechanical properties after ageing 200 °C for 3 h, in which the UTS and El are 416 MPa and 6.9%, respectively. After ageing at 300 °C for 3 h, the elongation increased significantly to 16.0 %.

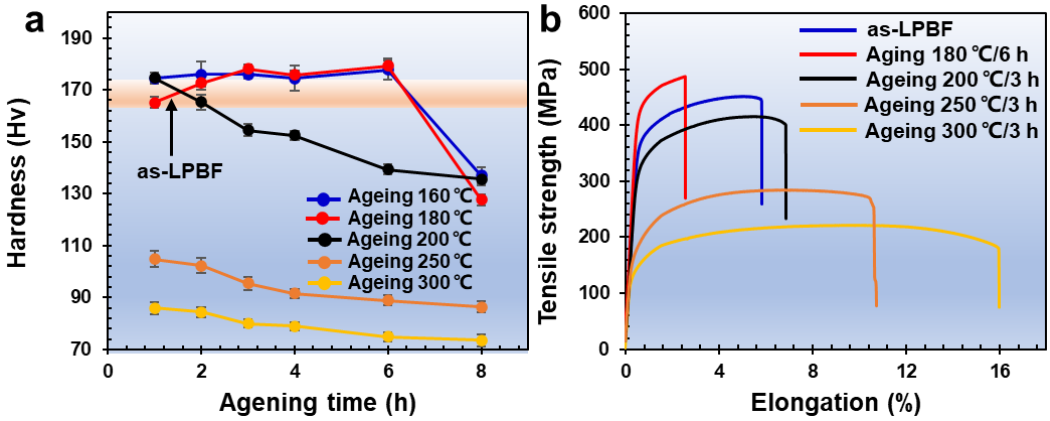

Fig. 11 (a) the Vickers hardness and (b) the tensile stress-strain curves of as-LPBFed Al-5.3Mg-3.3Si alloy without and with ageing treatments.

Table. 3 Mechanical properties of the as-LPBFed Al-5.3Mg-3.3Si alloys under different direct ageing conditions

Condition	Hardness (Hv)	YS (MPa)	UTS (MPa)	El (%)
as-LPBFed	170.8 ± 1.9	374 ± 6	452 ± 6	5.8 ± 0.4
Aged at 160 °C/6h	177.8 ± 2.7	428 ± 8	483 ± 9	1.8 ± 0.1
Aged at 180 °C/6h	179.2 ± 3.6	433 ± 6	487 ± 10	2.6 ± 0.2
Aged at 200 °C/1h	174.6 ± 2.2	401 ± 6	461 ± 10	2.7 ± 0.1
Aged at 200 °C/3h	154.5 ± 3.5	338 ± 5	416 ± 7	6.9 ± 0.3
Aged at 250 °C/3h	95.4 ± 2.4	173 ± 3	285 ± 5	10.7 ± 0.6
Aged at 300 °C/1h	80.2 ± 1.6	146 ± 2	242 ± 7	11.7 ± 0.5
Aged at 300 °C/3h	74.6 ± 1.7	140 ± 2	221 ± 3	16.0 ± 0.9

Fig. 12 shows the typical fracture morphology of as-LBPFed Al-5.3Mg-3.3Si alloy. In **Figs. 12b-c**, the fracture of the as-LBPFed sample was mainly composed of tearing ridges and dimples**.** The poor elongation of as-LPBFed sample aged at 180 °C for 6 h was mainly related to a brittle-plastic mixed fracture mode that contained shorter and shallower dimples, while

the superior elongation of as-LPBFed sample aged at 300 °C for 3 h was mainly relevant with the ductile fracture mode that contained deep and large equiaxed dimples.

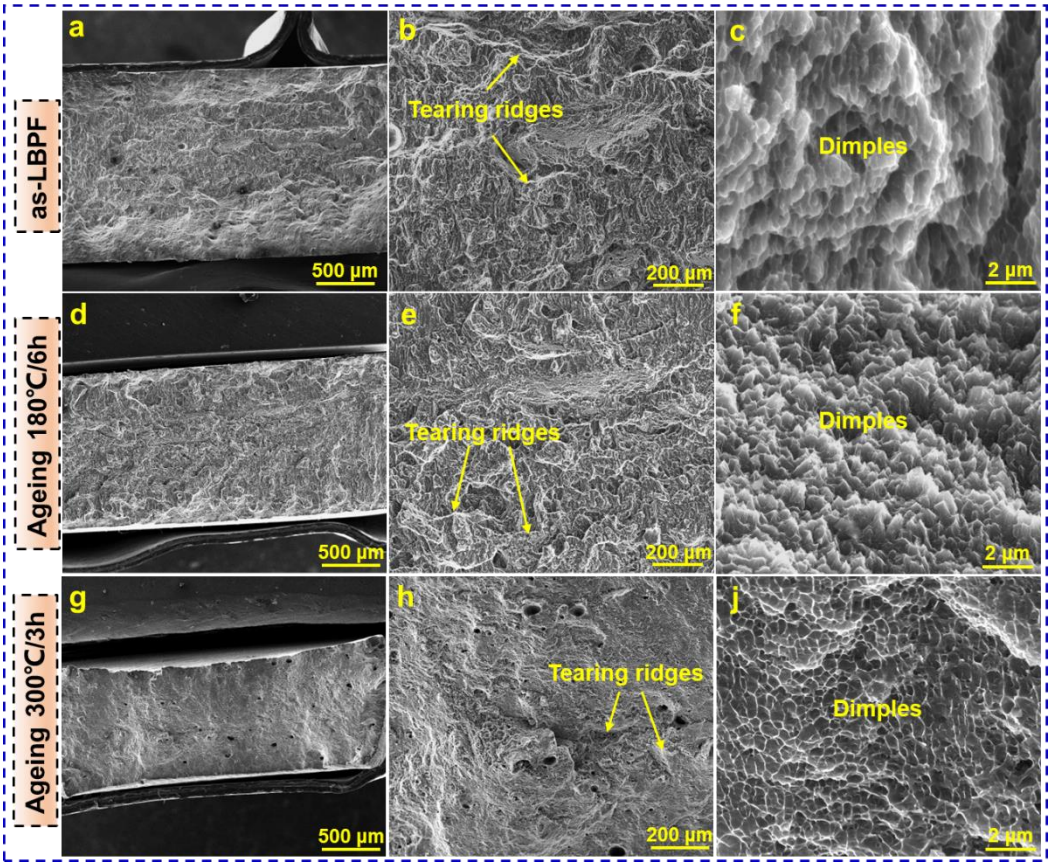

Fig. 12. SEM micrographs showing the fracture morphology of the as-LBPFed Al-5.3Mg-3.3Si alloy: (a-c) as-LPBFed state; (d-f) aged at 180 ºC for 6 h; (g-j) aged at 300 ºC for 3 h

4 Discussion

4.1 The processability of Al-5.3Mg-3.3Si alloy

Based on the cost 507 thermodynamic database, the vertical cross-section along the Al-5Mg-*x*Si was calculated. From **Fig. 13a**, Si promotes the formation of Mg_2Si, and eutectic Si phase starts to appear when the Si content exceeds 3.34 wt.%. The solidification sequence is: L → α-Al, L → (α-Al + Mg_2Si), L → (α-Al + Mg_2Si + Si). Mg_2Si and Si phases form when the temperature is below 585.3 °C and 554.3 °C, respectively. Generally, the most additively manufactured Al alloys exhibit hot cracking because of the rapid cooling rate and large temperature gradient during LPBF process[30, 31]. The index of $|dT/d(fs)^{1/2}|$ proposed by Kou can be used as a criterion for the cracks susceptibility. The index is closely linked to the steepness of the solidification curve under the condition of $(fs)^{1/2} = 1$. Therefore, the crack susceptibility of the alloy can be calculated from the solidification curve. In this work, the Scheil-Gulliver solidification curves of Al-5.3Mg-3.3Si and other widely-researched Al

alloys, including Al2024, Al6061 and Al7075 alloys were plotted in **Fig. 13b**. The narrow solidification range (64.8 °C) demonstrates that the Al-5.3Mg-3.3Si alloy tend to have a low crack susceptibility, which is consistent with the results of SEM and EBSD (**Fig. 5**). Additionally, combing the above experiment and calculation results, the low hot cracking susceptibility of the as-LPBF Al-5.3Mg-3.3Si alloy is also related to the formation of eutectic cellular structure, which improves liquid filling rate and resists cracking during LPBF process. A similar situation can be found in as-LPBFed Al-Si alloys [32].

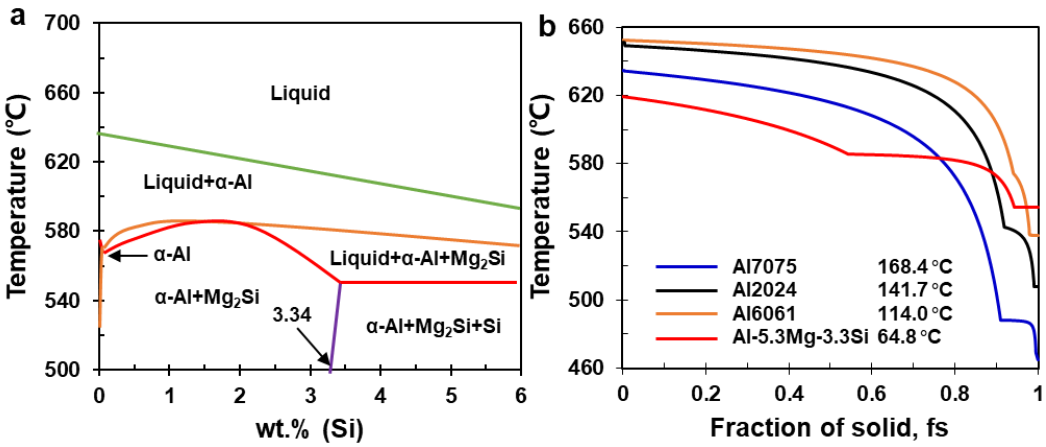

Fig. 13. (a) Vertical cross-section of Al-5Mg-*x*Si alloy; (b) the comparison of the solidification range between Al-5.3Mg-3.3Si and other widely-researched Al alloy, including Al2204, Al6061 and Al7075.

4.2 Microstructural evolution

The schematic of the microstructure evolution of as-LPBFed and as-aged Al-5.3Mg-3.3Si alloy is illustrated in **Fig. 14**. Under the as-LPBFed condition, the microstructures mainly consist of the interaction between Al/Mg_2Si eutectic cellular structure a high number density dislocation, which is closely related with the high strain induced via high cooling rates (10^5~10^6 K/s) and the thermal contraction stresses during LPBFed process [30, 33, 34]. After ageing at 180 °C for 6 h, the microstructural characteristics include that the interaction between the formation of Mg_2Si particles and the remained Al/Mg_2Si eutectic cellular structure with large size (~0.56 μm). In general, the basic precipitation sequence of Al-Mg-Si alloy is: SSS (supersaturated solid solution) → solute clusters → GPB zones → β″(Mg_5Si_6 or $Mg_5Al_2Si_4$) → β′($Al_3Mg_9Si_7$) → β [35]. TEM-EDS results in **Table 2** indicated that the concentration of Mg and Si reduced from ~ 2.2 wt.% and ~ 1.9 wt.% at LPBF state to ~ 0.8 wt.% and ~ 0.6 wt.% at the condition of ageing 180 °C for 3 h, which led to the precipitation of nano-sized β″ precipitate (**Fig. 9c, d**). Moreover, the β″ precipitates were further transformed to β phase with increasing ageing time (**Fig. 9e, f**). When the ageing temperature exceeds 300 °C, the feature of Al/Mg_2Si eutectic cellular structure are completely broken and

transformed into coarse Mg_2Si particles (~ 350 nm) in **Fig. 14c**, which similar to as-LPBFed Al-Si alloy[5].

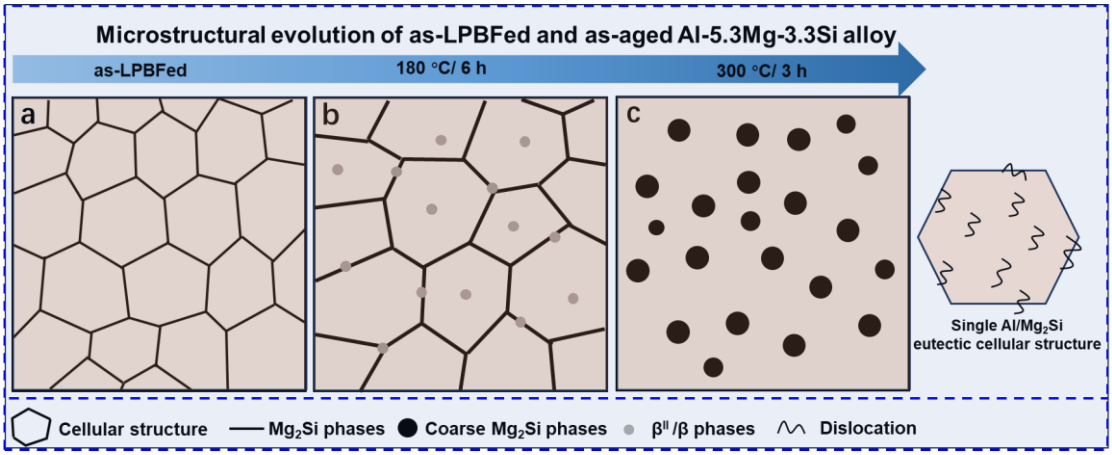

Fig. 14 Schematic of microstructural evolution of as-LPBFed and as-aged Al-5.3Mg-3.3Si alloy: (a) as-LPBFed; (b) 180 °C; (c) 300 °C

4.3 Strengthening mechanisms

To understand the variation of strength for the as-LPBFed and as-aged Al-5.3Mg-3.3Si alloys, it is essential to clarify the contributions of different strengthening mechanisms, which is closely related to evolution of grain size, content of solid solution, dislocation density and precipitation phases. Consequently, the main strengthening mechanisms involve the combination of grain boundary strengthening (σ_g), solid solution strengthening (σ_{ss}) dislocation strengthening (σ_{dis}) and precipitation strengthening (σ_p), in addition to its lattice friction strength σ_0. For simplicity, the contribution of main mechanisms responsible for strengthening can be expressed as:

$$\sigma_y = \sigma_0 + \sigma_g + \sigma_{cb} + \sigma_{dis} + \sigma_p \qquad (6)$$

where σ_0 is a constant (10 MPa for Al alloy[36])

(1) Grain boundary strengthening

The high cooling rate limits the growth of grains during solidification. The average grain size of the as-LPBFed and as-aged samples at 180 °C and 300 °C were 12.1 μm, 11.9 μm and 12.7 μm, respectively. The strengthening contribution of grain boundary strengthening can be estimated via the Hall-Petch relationship as follow:

$$\sigma_g = K \times d^{-1/2} \qquad (7)$$

where K is the Hall-Petch constant, which is determined to be 0.04 MPa $m^{1/2}$ from previous

literatures[37]. d is the average sizes of α-Al grain. The σ_g of the as-LPBFed and as-aged sample treated at 180 ºC are 12 MPa, 12 MPa and 11 MPa.

(2) Solid solution strengthening

The supersaturated solid solution of Mg and Si can be acquired during the rapid solidification of LPBF processing. The contribution of solid solution strengthening can be calculated as follow:

$$\sigma_{ss}=k_{Mg}C_{Mg}^{m}+k_{Si}C_{Si}^{m} \quad (8)$$

Where k_{Mg} and k_{Si} and M are 17 MPa/wt.%, 11 MPa/wt.% and 1[38], respectively. C_{Mg} and C_{Si} are the concentration of solution Mg and Si. Based on the STEM-EDS results in **Table 2**, the σ_{cc} of the as-LPBFed and as-aged sample treated at 180 ºC are 58 MPa and 20 MPa.

(3) Dislocation strengthening

The dislocation strengthening can be evaluated via the Bailey-Hirsch relation[39]

$$\sigma_{dis} = M\cdot\alpha\cdot G\cdot b\cdot\rho^{0.5} \quad (9)$$

where M is the Taylor factor (3.06 for FCC crystal structure of Al[20]), α is a material constant (0.2[40]), G is the shear modulus (26 GPa[41]), b is the Burgers vector (0.286 nm[26]), and ρ is the dislocation density. The ρ values of as-LPBFed and as-aged samples at 180 ℃ and 300 ℃ are 7.1×10^{14} m^{-2}, 6.2×10^{14} m^{-2} and 4.2×10^{14} m^{-2}. The strength contribution from dislocation strengthening to strength enhancement is evaluated as 121 MPa, 113 MPa and 93 MPa, respectively.

(4) Precipitation strengthening

A large number density of nano-sized particles detected in the as-LPBFed and as-aged Al-5.3Mg-3.3Si alloy have a coherent orientation relationship with α-Al, which makes a strong contribution to the Orowan strengthening (**Fig. 5a&Fig. 9a).** The formation of β″and β nanoparticles was closely related to the strength enhancement after direct ageing. The increment of yield strength by precipitation strengthening can be calculated through the Orowan by pass mechanism[42, 43]:

$$\sigma_p=\frac{0.4MGb}{\pi(1-\nu)^{\frac{1}{2}}}\times\frac{\ln(d/b)}{\lambda} \quad (10)$$

$$\lambda=\frac{1}{2}d\sqrt{3\pi/2f_v} \quad (11)$$

where v is the Poisson's ratio (0.33), d is the average diameter of the precipitates, λ is the spacing between the precipitates in the glide surface, which is associated with the diameter d and volume fraction f_v of the precipitates. According to the TEM and SEM results, the average diameter of Mg_2Si particles in as-LPBFed and as-aged samples treated at 180 °C and 300 °C are 27.4 nm, 58.8 nm and 177.5 nm. The f_v values are 9.5 %, 10.7 % and 12.5 %. The precipitation strengthening for the Mg_2Si particles was calculated as 161 MPa, 98 MPa and 41 MPa, respectively. Since the shape and size of β″ and β particles are similar, the d and f_v are measured together. The d and f_v of β″/β particles are 11.2 nm, and 2.1 % in as-aged samples at 180 °C, respectively. The precipitation strengthening for the β″/β particles was calculated as 155 MPa.

The multiple strengthening mechanisms can be calculated using equation (6). **Fig. 15** shows a comparison of contributions to yield strength between calculation and experimental measurement. According to the calculation, the yield strength of the as-SLMed alloy is 361 MPa, which is very close to the data obtained from experimental data (374 MPa). The solution Mg and Si, the nano-size Mg_2Si particles and a high number density of dislocations are the main contributors of the high strength. The precipitation of β″and β phase is the main reason for the strength enhancement after ageing at 180 °C for 6 h (~ 433 MPa). When the ageing temperature reach up to 300 °C, the softening reason can be attributed to the following aspects: (*i*) the absent of solid solution strengthening induced the precipitation of Mg and Si elements; (*ii*) the coarse Mg_2Si particles (~350 nm) leads to poor precipitation strengthening effect; (*iii*) the reduction of dislocation density weakens the effect of dislocation strengthening significantly.

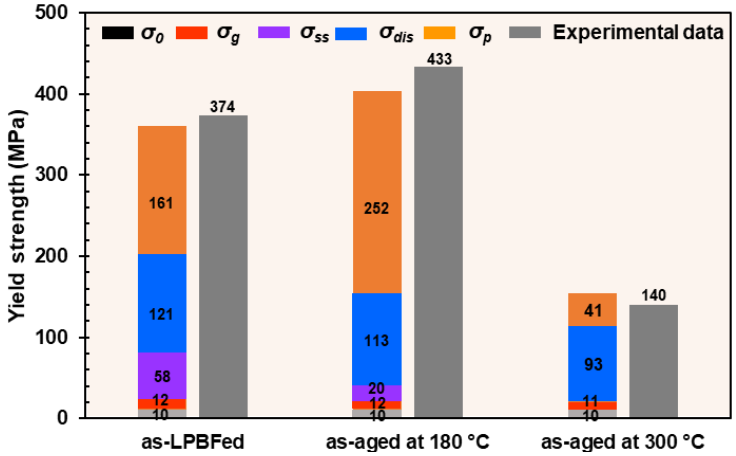

Fig. 15. A comparison of contributions to yield strength of Al-5.3Mg-3.3Si alloy between the calculation and the experimental measurement.

Fig. 16 shows a comparison between mechanical performance of as-LPBFed and as-aged alloys and other reported Al alloys, including casting Al-Mg-Si [44, 45], as-LPBFed and heat-

treated Al-Mg-Si [20-22], Al-Si-Mg [46-52], Al-Cu-Mg[53-56] and Al-Zn-Mg-Cu [57-59] alloys. It can be seen that the YS of as-LPBFed and as-aged Al-5.3Mg-3.3Si alloy was higher than those of cast Al-Mg-Si and Al-Si-Mg alloy. The Al-5.3Mg-3.3Si alloy also exhibits enhanced comprehensive mechanical properties in counterpart with currently studied as-LPBFed Al-Mg-Si alloys. Specifically, the YS of Al-5.3Mg-3.3Si alloy is comparable to or even higher than that of a part of Al-Cu-Mg and Al-Zn-Mg-Cu alloy. This alloy designed in this work does not contain Sc/Zr and nanoparticle, which makes it more suitable for various applications.

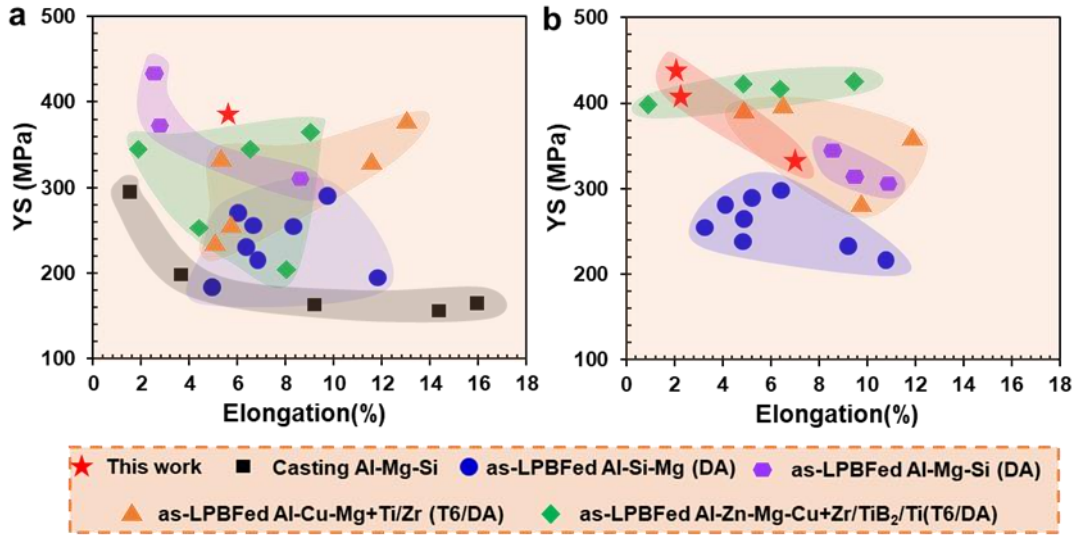

Fig. 16 Comparison of the YS of as-LPBFed alloy and other reported Al alloys, including casting Al-Mg-Si [44, 45], as-LPBFed and heat-treated Al-Mg-Si [20-22], Al-Si-Mg [46-52], Al-Cu-Mg [53-56] and Al-Zn-Mg-Cu [57-59] alloys: (a) as-LPBFed; (b) T6 treatment and direct ageing.

5. Conclusions

In this study, the Al-5.3Mg-3.3Si alloy has been designed and fabricated by LPBF successfully. The microstructural evolution and mechanical properties of as-LPBFed alloy without and with ageing treatment were investigated systematically, and the main conclusions are as follows:

(1) The as-LPBFed Al-5.3Mg-3.3Si alloy with a low solidification range of 64.8 °C exhibits a superior processability. The microstructure was composed of the Al/Mg_2Si eutectic cellular structure with a high number density of dislocations. The UTS, YS and El of as-LPBFed Al-5.3Mg-3.3Si alloy were 452 MPa, 374 MPa and 5.8%, respectively. The solution Mg and Si, the nano-sized Mg_2Si particles and the dislocation are the main contributors of the high strength.

(2) After ageing at 180 °C, the features of microstructure include that the Al/Mg_2Si eutectic

cellular structure remained and the nano-sized β′′ and β precipitate in the α-Al matrix. The UTS and YS increased to 487 MPa and 433 MPa. The precipitation of β′′ and β phase is the main reason for the strength enhancement

(3) When the ageing temperature exceeded 300 °C, the feature of Al/Mg_2Si eutectic cellular structure were completely broken and transformed into coarse Mg_2Si particles. The strength of the alloy was significantly reduced and the elongation increased to 16%. The softening mechanism is the coarsening of Mg_2Si phases and the reduction of dislocation density.

Credit authorship contribution statement

Tao Wen: Experiments, data collection and analysis, writing - original draft. **Jianying Wang:** Experiments and data analysis, writing - review. **Zhicheng Li:** Experiments and data collection. **Feipeng Yang:** Experiments and data analysis. **Zhilin Liu:** Conceptualization, writing – review & editing, supervision. **Hailin Yang:** Conceptualization, funding acquisition, project management, supervision, writing - editing & review. **Shouxun Ji:** Conceptualization, results review, writing - editing & review.

Declaration of Competing Interest

The authors declare that they have no known competing financial interests or personal relationships that could have appeared to influence the work reported in this paper.

Data availability

Data will be made available on request.

Acknowledgement

Financial support from the National Key Research and Development Program of China (Grant No. 2020YFB0311300ZL), and National Natural Science Foundation of China (Grant No. 52071343) are gratefully acknowledged.

References

[1] T. Sun, J. Chen, Y. Wu, M. Wang, Y. Fu, H. Wang, Achieving excellent strength of the LPBF additively manufactured Al-Cu-Mg composite via in-situ mixing TiB_2 and solution treatment, Mater. Sci. Eng. A. 850 (2022), 143531.

[2] T. DebRoy, H.L. Wei, J.S. Zuback, T. Mukherjee, J.W. Elmer, J.O. Milewski, A.M. Beese, A. Wilson-Heid, A. De, W. Zhang, Additive manufacturing of metallic components-process, structure and properties, Prog. Mater. Sci. 92 (2018) 112-224.

[3] J.Y. Wang, J.P. Zou, H.L. Yang, Z.L. Liu, S.X. Ji, High strength and ductility of an

additively manufactured CrCoNi medium-entropy alloy achieved by minor Mo doping, Mater. Sci. Eng. A 843 (2022) 143129.
[4] M. Garibaldi, I. Ashcroft, M. Simonelli, R. Hague, Metallurgy of high-silicon steel parts produced using selective laser melting, Acta Mater. 110 (2016) 207-216.
[5] N.T. Aboulkhair, M. Simonelli, L. Parry, I. Ashcroft, C. Tuck, R. Hague, 3D printing of aluminium alloys: additive manufacturing of aluminium alloys using selective laser melting, Prog. Mater. Sci. 106 (2019), 100578.
[6] N. Kaufmann, M. Imran, T.M. Wischeropp, C. Emmelmann, S. Siddique, F. Walther, Influence of process parameters on the quality of aluminium alloy EN AW 7075 using selective laser melting (SLM), Phys. Procedia. 83 (2016) 918-926.
[7] M. Opprecht, J.P. Garandet, G. Roux, C. Flament, M. Soulier, A solution to the hot cracking problem for aluminium alloys manufactured by laser beam melting, Acta Mater. 197 (2020) 40-53.
[8] M. Doubenskaia, A. Domashenkov, I. Smurov, P. Petrovskiy, Study of selective laser melting of intermetallic TiAl powder using integral analysis, Int. J. Mach. Tool. Manu. 129 (2018) 1-14.
[9] J. Suryawanshi, K.G. Prashanth, S. Scudino, J. Eckert, O. Prakash, U. Ramamurty, Simultaneous enhancements of strength and toughness in an Al-12Si alloy synthesized using selective laser melting, Acta Mater. 115 (2016) 285-294.
[10] X.P. Li, X.J. Wang, M. Saunders, A. Suvorova, L.C. Zhang, Y.J. Liu, M.H. Fang, Z.H. Huang, T.B. Sercombe, A selective laser melting and solution heat treatment refined Al-12Si alloy with a controllable ultrafine eutectic microstructure and 25% tensile ductility, Acta Mater. 95 (2015) 74-82.
[11] L. Thijs, K. Kempen, J.P. Kruth, J.V. Humbeeck, Fine-structured aluminium products with controllable texture by selective laser melting of pre-alloyed AlSi10Mg powder, Acta Mater. 61 (5) (2013) 1809-1819.
[12] I. Rosenthal, R. Shneck, A. Stern, Heat treatment effect on the mechanical properties and fracture mechanism in AlSi10Mg fabricated by additive manufacturing selective laser melting process, Mater. Sci. Eng., A. 729 (2018) 310-322.
[13] J.H. Martin, B.D. Yahata, J.M. Hundley, J.A. Mayer, T.A. Schaedler, T.M. Pollock, 3D printing of high-strength aluminium alloys, Nature. 549 (2017) 365-369.
[14] D. Liu, H.V. Atkinson, P. Kapranos, W. Jirattiticharoean, H. Jones, Microstructural evolution and tensile mechanical properties of thixoformed high performance aluminium alloys, Mater. Sci. Eng., A. 361 (1-2) (2003) 213-224.
[15] J. Deng, C. Chen, W. Zhang, Y. Li, R. Li, K. Zhou, Densification, microstructure, and

mechanical properties of additively manufactured 2124 Al-Cu alloy by selective laser melting, Materials. 13 (19) (2020), 4423.
[16] S. Wu, Z. Lei, B. Li, J. Liang, Y. Chen, Hot cracking evolution and formation mechanism in 2195 Al-Li alloy printed by laser powder bed fusion, Addit. Manuf. 54 (2022), 102762.
[17] R. Li, M. Wang, Z. Li, P. Cao, T. Yuan, H. Zhu, Developing a high-strength Al-Mg-Si-Sc-Zr alloy for selective laser melting: crack-inhibiting and multiple strengthening mechanisms, Acta Mater. 193 (2020) 83-98.
[18] M. Qu, Q. Guo, L.I. Escano, A. Nabaa, S.M.H. Hojjatzadeh, Z.A. Young, L. Chen, Controlling process instability for defect lean metal additive manufacturing, Nat. Commun. 13 (1) (2022), 1079.
[19] M. Opprecht, J.P. Garandet, G. Roux, C. Flament, An understanding of duplex microstructures encountered during high strength aluminium alloy laser beam melting processing, Acta Mater. 215 (2021), 117024.
[20] F Li, Z.C. Li, C.L. Tang, L.J. Zhang, Q.Y. Tan, C. Chen, M.X. Zhang, K.C. Zhou, Design high-strength Al–Mg–Si alloy fabricated by laser powder bed fusion: Cracking suppression and strengthening mechanism, Mater. Sci. Eng., A. 864 (2023) 144591.
[21] F.P. Yang, J.Y. Wang, T. Wen, X. Ai, X.X. Dong, H.L. Yang, S.X. Ji, Microstructure and mechanical properties of pseudo binary eutectic Al–Mg_2Si alloy processed by laser powder bed fusion, J. Mater. Res. Technol. 24 (2023), 2187-2199.
[22] J.Y. Wang, F.P. Yang, H.L. Yang, L.J. Zhang, Y.Y. Zhang, Z.L. Liu, S.X. Ji, Effect of heat treatment on the microstructure and mechanical properties of an Al-5Mg2Si-2Mg alloy processed by laser powder bed fusion, J. Alloys Compd. 920 (2022) 165944.
[23] W. Li, S. Li, J. Liu, A. Zhang, Y. Zhou, Q.S. Wei, C.Z. Yan, Y.S. Shi, Effect of heat treatment on AlSi10Mg alloy fabricated by selective laser melting: Microstructure evolution, mechanical properties and fracture mechanism, Mater. Sci. Eng., A. 663 (2016), 116-125.
[24] T.H. Park, M.S. Baek, H. Hyer, Y.H. Sohn, K.A. Lee, Effect of direct ageing on the microstructure and tensile properties of AlSi10Mg alloy manufactured by selective laser melting process, Mater. Charact. 176 (2021) 111113.
[25] Y.X. Geng, Q. Wang, Y. Wang, Q. Zang, S. Mi, J. Xu, Y. Xiao, Y. Wu, J. Luan, Microstructural evolution and strengthening mechanism of high-strength AlSi8.1Mg1.4 alloy produced by selective laser melting, Mater. Des. 218 (2022), 110674.
[26] S. Malopheyev, V. Kulitskiy, R. Kaibyshev, Deformation structures and strengthening mechanisms in an Al-Mg-Sc-Zr alloy, J. Alloys Compd. 698 (2017) 957-966.
[27] J.Y. He, H. Wang, H.L. Huang, X.D. Xu, M.W. Chen, Y. Wu, X.J. Liu, T.G. Nieh, K. An,

Z. P. Lu, A precipitation-hardened high-entropy alloy with outstanding tensile properties, Acta Mater. 102 (2016) 187-196.
[28] M.J. Yang, A. Orekhov, Z.Y. Hu, M. Feng, S.B. Jin, G. Sha, K. Li, V. Samaee, M. Song, Y. Du, G.V. Tendeloo, D. Schryvers, Shearing and rotation of β″ and β′ precipitates in an Al-Mg-Si alloy under tensile deformation: In-situ and ex-situ studies, Acta Mater. 220 (2021), 117310.
[29] Y.F. Wang, Y.L. Lu, S.Y. Zhang, H.P. Zhang, H. Wang, Z, Characterization and strengthening effects of different precipitates in Al–7Si–Mg alloy, J. Alloys Compd. 885 (2021), 161028.
[30] J. Zhang, B. Song, Q. Wei, D. Bourell, Y. Shi, A review of selective laser melting of aluminum alloys: processing, microstructure, property and developing trends, J. Mater. Sci. Technol. 35 (2) (2019) 270-284.
[31] S. Kou, A criterion for cracking during solidification, Acta Mater. 88 (2015) 366-374.
[32] Y. Bai, Y. Yang, Z. Xiao, M. Zhang, D. Wang, Process optimization and mechanical property evolution of AlSiMg0.75 by selective laser melting, Mater. Des. 140 (2018) 257-266.
[33] H.R. Kotadia, A. Professor, G. Gibbons, A. Das, P.D. Howes, A review of Laser Powder Bed Fusion Additive Manufacturing of aluminium alloys: Microstructure and properties, Addit. Manuf. 46 (2021) 102155.
[34] K.M. Bertsch, G. Meric de Bellefon, B. Kunehl, D.J. Thoma, Origin of dislocation structures in an additively manufactured austenitic stainless steel 316L, Acta Mater. 199 (2020) 19-33.
[35] J. Fiocchi, A. Tusissi, C.A. Biffi. Heat treatment of aluminium alloys produced by laser powder bed fusion: A review, Mater. Des. 204 (2021) 109651.
[36] J.Y. Wang, J.B. Gao, H.L. Yang, F.P. Yang, T. Wen. Z.L. Liu, L.J. Zhang, S.X. Ji, High-strength Al-5Mg2Si-2Mg-2Fe alloy with extremely high Fe content for green industrial application through additive manufacturing, Virtual. Phys. Prototy. 18 (2023) 2235587.
[37] N. Hansen, Hall–Petch relation and boundary strengthening, Scr. Mater. 51 (8) (2004) 801-806.
[38] Z. Feng, X.M. Wang, H. Tan, F.Y. Zhang, W. Fan, Y.X. Wang, Y.B. Fang, J.L. Wang, F. Wu, X. Lin, W.D. Huang, Effect of heat treatment patterns on porosity, microstructure, and mechanical properties of selective laser melted TiB2/Al–Si–Mg composite, Mater. Sci. Eng., A. 855 (2022), 143932.
[39] J.Y. Wang, J.P. Zou, H.L. Yang, X.X. Dong, P. Cao, X.Z. Liao, Z.L. Liu, S.X. Ji, Ultrastrong and ductile (CoCrNi)94Ti3Al3 medium-entropy alloys via introducing multi-scale heterogeneous structures, J. Mater. Sci. Tech. 135 (2023) 241-249.

[40] K. Ma, H. Wen, T. Hu, T. D. Topping, D. Isheim, D. N. Seidman, E. J. Lavernia, J. M. Schoenung, Mechanical behavior and strengthening mechanisms in ultrafine grain precipitation-strengthened aluminum alloy, Acta Mater. 62 (2014) 141-155.
[41] E.L. Huskins, B. Cao, K.T. Ramesh, Strengthening mechanisms in an Al-Mg alloy, Mater. Sci. Eng., A. 527 (6) (2010) 1292-1298.
[42] Z. Hu, H. Zhang, H. Zhu, Z. Xiao, X. Nie, X. Zeng, Microstructure, mechanical properties and strengthening mechanisms of AlCu5MnCdVA aluminum alloy fabricated by selective laser melting, Mater. Sci. Eng., A. 759 (2019) 154-166.
[43] F.P. Yang, J.Y. Wang, T. Wen, L. Zhang, X.X. Dong, D. Qiu, H. Yang, S.X. Ji, Developing a novel high-strength Al-Mg-Zn-Si alloy for laser powder bed fusion, Mater. Sci. Eng., A. 851 (2022), 143636.
[44] S. Ji, F. Yan, Z. Fan, Development of a high strength Al-Mg_2Si-Mg-Zn based alloy for high pressure die casting, Mater. Sci. Eng., A. 626 (2015) 165-174.
[45] X. Zhu, H. Yang, X. Dong, S. Ji, The effects of varying Mg and Si levels on the microstructural inhomogeneity and eutectic Mg_2Si morphology in die-cast Al-Mg-Si alloys, J. Mater. Sci. 54 (2019) 5773-5787.
[46] T. Kimura, T. Nakamoto, Microstructures and mechanical properties of A356 (AlSi7Mg0.3) aluminum alloy fabricated by selective laser melting, Mater. Des. 89 (2016) 1294-1301.
[47] J.H. Rao, Y. Zhang, K. Zhang, X. Wu, A. Huang, Selective laser melted Al-7Si-0.6Mg alloy with in-situ precipitation via platform heating for residual strain removal, Mater. Des. 182 (2019), 108005.
[48] Z.H. Xiong, S.L. Liu, S.F. Li, Y. Shi, Y.F. Yang, R.D.K. Misra, Role of melt pool boundary condition in determining the mechanical properties of selective laser melting AlSi10Mg alloy, Mater. Sci. Eng., A. 740-741 (2019) 148-156.
[49] F. Sajadi, J.M. Tiemann, N. Bandari, A.C. Darabi, J. Mola, S. Schmauder, Fatigue improvement of AlSi10Mg fabricated by laser-based powder bed fusion through heat-treatment, Metals. 11 (5) (2021), 683.
[50] H.P. Tang, C.F. Gao, Y. Zhang, N.N. Zhang, C. Lei, Y.J. Bi, P. Tang, J.H. Rao, Effects of direct aging treatment on microstructure, mechanical properties and residual stress of selective laser melted AlSi10Mg alloy, J. Mater. Sci. Technol. 139 (2023) 198-209.
[51] H. Zhang, Y. Wang, J.J. Wang, D.R. Ni, D. Wang, B.L. Xiao, Z.Y. Ma, Achieving superior mechanical properties of selective laser melted AlSi10Mg via direct aging treatment, J. Mater. Sci. Technol. 108 (2023) 226-235.

[52] S.M. Zhu, I. Katti, D. Qiu, J.H. Forsmark, M.A. Easton, Microstructural analysis of the influences of platform preheating and post-build heat treatment on mechanical properties of laser powder bed fusion manufactured AlSi10Mg alloy, Mater. Sci. Eng., A. 882 (2023), 145486.
[53] P. Wang, C. Gammer, F. Brenne, K.G. Prashanth, R.G. Mendes, M.H. Rümmeli, T. Gemming, J. Eckert, S. Scudino, Microstructure and mechanical properties of a heat-treatable Al-3.5Cu-1.5Mg-1Si alloy produced by selective laser melting, Mater. Sci. Eng., A. 711 (2018) 562-570.
[54] Q.Y. Tan, J.Q. Zhang, Q. Sun, Z.Q. Fan, G. Li, Y. Yin, Y.G. Liu, M.X. Zhang, Inoculation treatment of an additively manufactured 2024 aluminum alloy with titanium nanoparticles, Acta Mater 196 (2020) 1-16.
[55] Y.F. Wang, X. Lin, N. Kang, Z.H. Wang, Y.X. Liu, W.D. Huang, Influence of post-heat treatment on the microstructure and mechanical properties of Al-Cu-Mg-Zr alloy manufactured by selective laser melting, J. Mater. Sci. Technol. 111 (2022) 35-48.
[56] J.H. Wang, S.L. Zhang, R.Y. Lu, H. Yan, X.F. Li, D.H. Yi, X.H. Yang, B. Liu, H. Xu, P.K. Bai, A crack-free and high-strength Al-Cu-Mg-Mn-Zr alloy fabricated by laser powder bed fusion, Mater. Sci. Eng., A. 27 (2022) 143731.
[57] R. Casati, M. Coduri, M. Riccio, A. Rizzi, M. Vedani, Development of a high strength Al–Zn–Si–Mg–Cu alloy for selective laser melting, J. Alloys Compd. 801 (2019) 243-253.
[58] S.Y. Zhou, Y. Su, H. Wang, J. Enz, T. Ebel, M. Yan, Selective laser melting additive manufacturing of 7xxx series Al-Zn-Mg-Cu alloy: Cracking elimination by co-incorporation of Si and TiB2, Addit. Manuf. 36 (2020), 101458.
[59] Q.Y. Tan, Z.Q. Fan, X.Q. Tang, Y. Yin, G. Li, D.N. Huang, J.Q. Zhang, Y.G. Liu, F. Wang, T. Wu, X.L. Yang, H. Huang, Q. Zhu, M.X. Zhang, A novel strategy to additively manufacture 7075 aluminum alloy with selective laser melting, Mater. Sci. Eng., A. 821 (2021), 141638.